AFGWC/TN-81/003

AD A130201

CLOUD/CLEAR/SNOW ANALYSIS BASED ON SATELLITE DATA

By

MAJ ROBERT C. WORONICZ

MAY 1981

UNITED STATES AIR FORCE
AIR WEATHER SERVICE (MAC)
AIR FORCE GLOBAL WEATHER CENTRAL
OFFUTT AFB NE 68113

REVIEW AND APPROVAL STATEMENT

This publication approved for public release. There is no objection to unlimited distribution of this document to the public at large, or by the Defense Technical Information Center (DTIC) or to the National Technical Information Service (NTIS).

This technical publication has been reviewed and is approved for publication.

Charles W Cook

CHARLES W. COOK, GM-13
Reviewing Official

FOR THE COMMANDER

James Kerlin

JAMES KERLIN, Colonel, USAF
Chief, Technical Services Division

UNCLASSIFIED
SECURITY CLASSIFICATION OF THIS PAGE (When Data Entered)

REPORT DOCUMENTATION PAGE

READ INSTRUCTIONS BEFORE COMPLETING FORM

1. REPORT NUMBER: AFGWC/TN-81/003	2. GOVT ACCESSION NO.: AD A130 302
3. RECIPIENT'S CATALOG NUMBER:	
4. TITLE (and Subtitle): Cloud/Clear/Snow Analysis Based on Satellite Data	5. TYPE OF REPORT & PERIOD COVERED:
	6. PERFORMING ORG. REPORT NUMBER:
7. AUTHOR(s): Major Robert C. Woronicz	8. CONTRACT OR GRANT NUMBER(s):
9. PERFORMING ORGANIZATION NAME AND ADDRESS: HQ Air Force Global Weather Central (MAC), Offutt AFB, Nebraska 68113	10. PROGRAM ELEMENT, PROJECT, TASK AREA & WORK UNIT NUMBERS:
11. CONTROLLING OFFICE NAME AND ADDRESS: HQ Air Force Global Weather Central (MAC), Offutt AFB, Nebraska 68113	12. REPORT DATE: May 1981
	13. NUMBER OF PAGES: 44 + vi
14. MONITORING AGENCY NAME & ADDRESS(if different from Controlling Office): HQ Air Force Global Weather Central (MAC), Offutt AFB, Nebraska 68113	15. SECURITY CLASS. (of this report): Unclassified
	15a. DECLASSIFICATION/DOWNGRADING SCHEDULE: N/A

16. DISTRIBUTION STATEMENT (of this Report)
Approved for public release, distribution unlimited.

17. DISTRIBUTION STATEMENT (of the abstract entered in Block 20, if different from Report)
N/A

18. SUPPLEMENTARY NOTES

19. KEY WORDS (Continue on reverse side if necessary and identify by block number)
Cloud Analysis
Satellite Data
Nephanalysis
Objective Analysis
Snow Analysis

20. ABSTRACT (Continue on reverse side if necessary and identify by block number)
This technical note describes an automated cloud/clear/snow analysis technique that was developed at the Air Force Global Weather Central (AFGWC) to evaluate the performance of the Defense Meteorological Satellite Program (DMSP) Snow/Cloud Special Sensor (SSC). The evaluation demonstrated that cloud/clear/snow areas could be analyzed with a high degree of reliability.

DD FORM 1 JAN 73 1473 EDITION OF 1 NOV 65 IS OBSOLETE

UNCLASSIFIED
SECURITY CLASSIFICATION OF THIS PAGE (When Data Entered)

PREFACE

This technical note describes a study performed at the Air Force Global Weather Central (AFGWC) to evaluate the performance of an experimental meteorological satellite sensor. This sensor images the earth using reflected solar energy in the near-infrared portion of the spectrum. The emphasis is on the reliability of an automated technique which uses this and matching visual imagery to detect clouds. This technical note is intended to serve as a reference for future research and technical development. In addition, it provides useful information for the meteorological community at large.

This publication would not have been completed without the help of many people:

Mr Albert W. Kimball, Westinghouse Electric Corporation, for his brilliant advice and many contributions given throughout the project.

Major Kenneth P. Freeman, formerly AFGWC/TSIT, for his tremendous support, guidance and encouragement throughout the project.

Captain Don Janssen, AFGWC/ADSS, for his help in archiving and displaying digital satellite imagery.

The following members of the Target Acquisition Section, AFGWC/TSIT, for their assistance with the cloud analysis portion of the project:

Major Kenneth P. Freeman,
Major Arnold L. Friend,
Captain Kenneth E. Mitchell,
Captain Thomas P. Walters.

The many people of the 544th Strategic Intelligence Wing, Target Materials Squadron, Photographic Services Branch, for the outstanding, timely and professional photographic support, which was a key element in the preparation of this technical note.

The following reviewers for their very valuable comments and suggestions:

Mr Arthur W. Gulliver, AFGWC/DO,
Colonel Serhij Pilipowskyj, AFGWC/WS,
Lieutenant Colonel William S. Irvine, Jr., formerly AFGWC/TSI,
Lieutenant Colonel Lyman L. Kaiser, AFGWC/DOX,
Lieutenant Colonel Ronald L. Lininger, AFGWC/TSA,
Major Arnold L. Friend, AFGWC/TSIT,
Captain Kenneth E. Mitchell, AFGWC/TSIT,
Captain Thomas P. Walters, AFGWC/TSIT.

The following members of the Word Processing Center for their administrative support:

Mary Ann Kosmicki,
Ruth M. Drummond,
Rhonda Fischer,
Melissa Hockman.

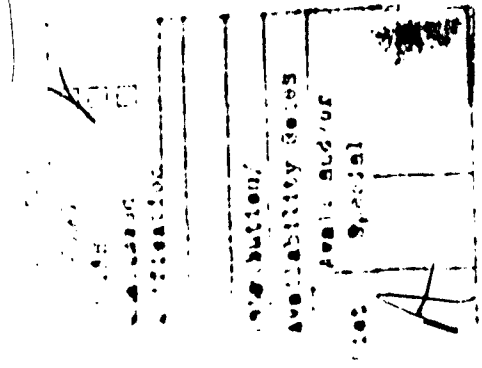

MAJOR ROBERT C. WORONICZ
21 May 1981

TABLE OF CONTENTS

LIST OF TABLES

LIST OF FIGURES

LIST OF ACRONYMS

AFGWC	Air Force Global Weather Central
BB	Black Body
BPI	Bits per inch
DF	Data Formatter
DMSP	Defense Meteorological Satellite Program
F4	DMSP flight four
FOV	Field of view
IFOV	Instantaneous field of view
IR	Infrared
L	Light energy
NESS	National Earth Satellite Service
NOAA	National Oceanic and Atmospheric Administration
OLS	DMSP Operational Linescan System
SD	Space Division
SNODEP	AFGWC Snow Cover Analysis Model
SSC	DMSP Snow/Cloud Special Sensor
T	Thermal infrared energy
WEC	Westinghouse Electric Corporation
WX5539	DMSP spacecraft number 5539
3DNEPH	AFGWC Three-Dimensional Nephanalysis Model

SECTION 1 - INTRODUCTION

The AFGWC automated cloud analysis model has been operational since January 1970. This model, known as the Three-Dimensional Nephanalysis (3DNEPH), relies heavily on meteorological satellites to provide cloud information over the entire world. Using the albedo and temperature data inferred from reflected light and emitted infrared imagery, respectively, the model is able to measure accurately the amount of cloudiness in individual cloud layers. The accuracy of this technique is far less reliable in polar and temperate zone winter regions than elsewhere. In these regions, snow and ice fields are virtually indistinguishable from low level clouds in both spectral bands. However, several investigators suggested that near-infrared and visible band sensors might be used to improve snow/cloud discrimination. As a result, the Defense Meteorological Satellite Program (DMSP) Program Office funded the design and development of a unique, inexpensive orbital instrument to exploit this new technology. We were designated as the office of primary responsibility for developing and testing new snow/cloud discrimination techniques as part of the on-orbit operation of the instrument. Our objectives were as follows:

Collect and evaluate data from the DMSP Snow/Cloud Special Sensor (SSC) to test the hypothesis that snow/cloud scene discrimination is possible through interpretation of a combination of SSC and DMSP Operational Linescan System (OLS) data.

List potential benefits if cloud and snow information is extracted from SSC-type imagery and processed by existing models.

We discuss the characteristics of the instruments in Section 2 and provide a detailed description of our data evaluation in Section 3. Section 4 reports the factors which limited the utility of the sensors. We list our conclusions and the potential benefits of processing near-infrared satellite data in Sections 5 and 6, respectively. Section 7 is a list of references.

SECTION 2 - INSTRUMENTATION

2.1 OPERATIONAL LINESCAN SYSTEM (OLS)

The OLS is a dual channel scanning radiometer which collects reflected light (L) and emitted thermal (T) infrared energy in the 0.4 to 1.1 um and 10.2to 12.8 um spectral bands, respectively. Energy is captured by a scanning telescope system driven in a sinusoidal motion by counter-reacting coiled springs and pulsed motor. The incoming beam of energy is split into two separate paths and then focused onto discrete L- and T-detector elements. The system moves the instantaneous field of view (IFOV) of these elements across the subtrack with maximum scanning velocity at nadir and reversals at the edge of scan. The angular IFOV is changed dynamically at selected portions of scan in order to maintain near constant resolution.

Electronic gain state settings are used to adjust L-detector sensitivity to approximate changes in solar irradiance caused by variation of solar zenith angle within the swath. The L-detector is designed to produce an output signal strength directly proportional to incoming scene radiance. This output is digitized into one of 128 possible greyshade values (i.e., 7 bits). These greyshades are truncated upon receipt at AFGWC to one of 64 possible greyshade values (6 bits).

The T-detector is designed to produce an output signal strength directly proportional to the equivalent Black Body (BB) temperature contained within the IFOV. However, atmospheric attenuation reduces incoming radiance so that equivalent BB temperatures are less than temperatures of radiating surfaces. Figure 2.1 contains a plot of average ambient air temperature versus matching T-detector output for clear scenes. The detector response is digitized into one of 128 possible greyshade values (7 bits). These greyshades are truncated upon receipt at AFGWC to one of 64 possible greyshade values (6 bits).

The L- and T-detector data are received in near constant 1.5 nm resolution at AFGWC where they are smoothed spatially to a near constant 3.0 nm resolution. The resultant light and thermal IR band data are copied to 7-track, 800 BPI magnetic tapes. Beginning October 1979, L- and T-detector data were saved from one orbital revolution each day for this study.

2.2 SNOW/CLOUD SPECIAL SENSOR (SSC)

The SSC is a narrow spectral band, staring mode, "push broom" scanning radiometer. This radiometer is a 48 element linear array of germanium photovoltaic detector elements which lies in the image plane of a 40.2° wide angle lens designed to provide constant angular field of view (FOV) per array element (14.6 mrad along track, 9.61 mrad cross track on 14.6 mrad centers). The instrument's FOV extends from subtrack toward the sun and covers about 400 nm on the earth's surface. Figure 2.2 shows the nominal detector footprint.

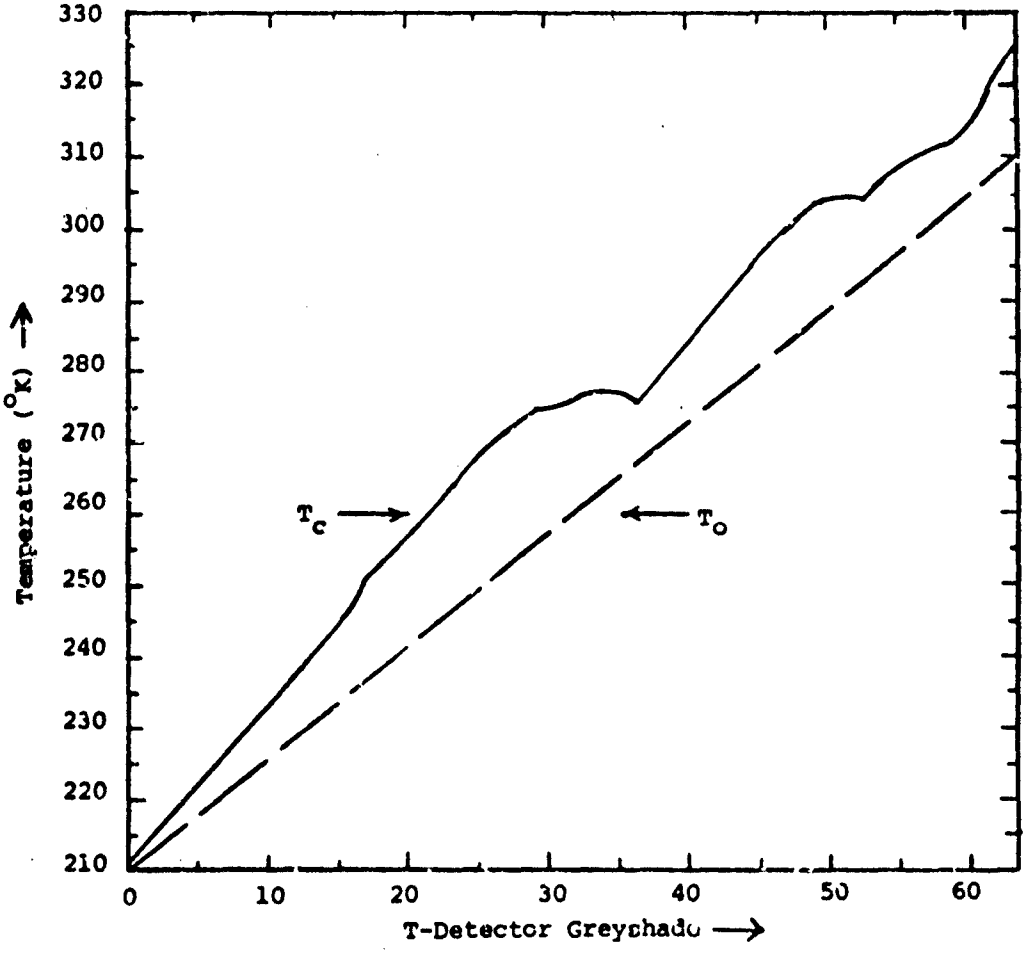

Figure 2.1. Plots of average apparent Black Body temperature (T_o) from clear radiating surfaces and corresponding average ambient air temperatures (T_c) versus matching T-detector greyshade values.

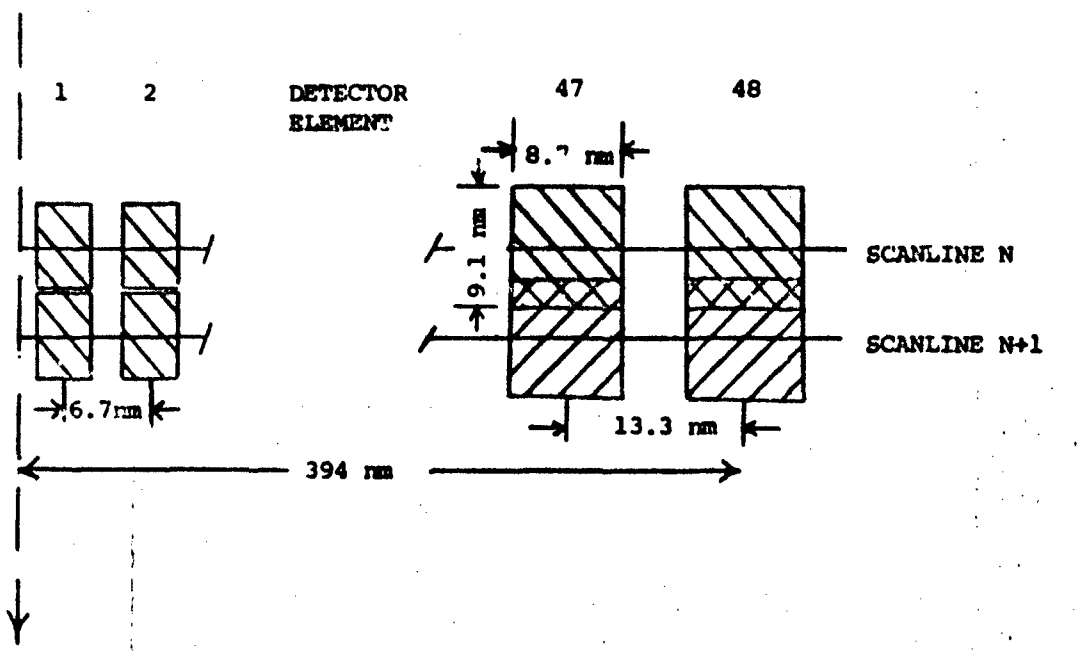

Figure 3.2. SSC footprint at nominal DMSP altitude.

The instrument collects reflected solar energy in the 1.51 to 1.63 um spectral band for input signal strength. Sixteen gain states, spaced at 2.4 dB, are available for use at specified programmed times along the orbital track. They are used to compensate approximately for variations in scene illumination from near subsolar to terminator regions. Channels are sampled in the "push broom" mode every two seconds and are individually digitized to six bits (64 possible greyshades). These data are recorded on the spacecraft, relayed to DMSP Control and Readout Stations, shipped to AFGWC, reformatted and recorded on tape with standard time and ephemeris information. Table 2.1 provides additional sensor design information.

ITEM	VALUE	UNITS
Number of Channels	48	-
Spectral Band	1.51 to 1.63	μm
Output Data Quantization	6	Bits
Data Frame Time	2	sec
Each Channel Time Constant	0.68	sec
Multiplex Time per Channel	10	msec
IFOV each Channel	14.6 x 9.1	mrad
Power Consumption	10.86	watts
Weight	8.58	lbs

Table 2.1. SSC System Parameters.

SECTION 3 - DATA EVALUATION

We began early orbit check-out of SSC shortly after launch of DMSP WX5539, flight four (F4), on 6 June 1979. Although the sensor was in good working order, Westinghouse Electric Corporation (WEC) engineers reported that the ambient sensor temperature was slightly higher than desired. This high temperature had negligible impact on sensor performance. Based on our findings and a thorough evaluation by system engineers, Space Division (SD) declared the SSC operational on 10 June 79.

Shortly thereafter, system engineers uploaded a pre-programmed gain state profile to compensate for variations in scene illumination throughout the orbital path. As a result, the detectors produced full scale output (saturation) whenever scene reflectances (assuming Lambertian surfaces) exceeded 23%.

When we compared printer plots of SSC data to transparencies of matching 1.5 nm resolution DMSP light data, we noticed that the sensor usually saturated if liquid water clouds filled the FOV. The SSC output from snow-filled FOVs indicated that reflectivities were 6%. The dynamic range of the sensor was sufficiently wide to handle cloud-free, snow-free scene radiances over a wide variety of geographic features. However, the detector was saturating over both arid and semi-arid scenes. We felt that liquid water cloud reflectivities and arid scene reflectivities could be equivalent under certain conditions. However, we could not study this aspect without expanding the dynamic range of the sensor. If these reflectivities were nearly equivalent then the task of developing reliable cloud/no cloud decision algorithms for worldwide use could be extremely difficult. We decided to identify areas in the world where reflectivities were a potential problem and to develop a new gain state profile to expand the dynamic range.

To observe worldwide cloud-free reflectivities, we considered developing software to determine where cloud-free SSC data were acquired. We also considered using nephanalyses produced by the 3DNEPH model to make these determinations. Both of these approaches were ruled out because the manpower and computer costs would have been extremely high. We could get comparable results at a much smaller cost by computing minimum SSC brightness worldwide. The SSC minimum brightness is equal to detector response from cloud-free features, except in those cases where cirrus clouds are less reflective than arid terrain features. We developed software to compute minimum SSC brightness on an AFGWC eighth-mesh scale (25 nm grid spacing at 60°N). We used July and August 1979 SSC data to prepare a SSC minimum brightness data base and displayed the results on a photographic transparency (Figure 3.1). SSC digital responses were represented by 16 possible greyshade values, where black and white correspond to minimum and maximum responses, respectively. We identified areas in North Africa, the Middle East, Soviet Union, Mexico, and the United States where reflectivities were sufficiently high to cause the sensor to saturate.

Figure 3.1. A display of SSC minimum brightness (next page) based on SSC data collected during July and August 1979. Brightness is represented by 16 grey-shade values ranging from black to white. The sensor was set to produce full-scale output whenever scene reflectances exceeded approximately 23%. The white disk at the pole is merely a data void area. Notice that semi-arid and arid terrain features produced full-scale output. Snow-covered Greenland is much darker in comparison to the semi-arid regions by virtue of the low refectivity of snow in the near-infrared portion of the spectrum.

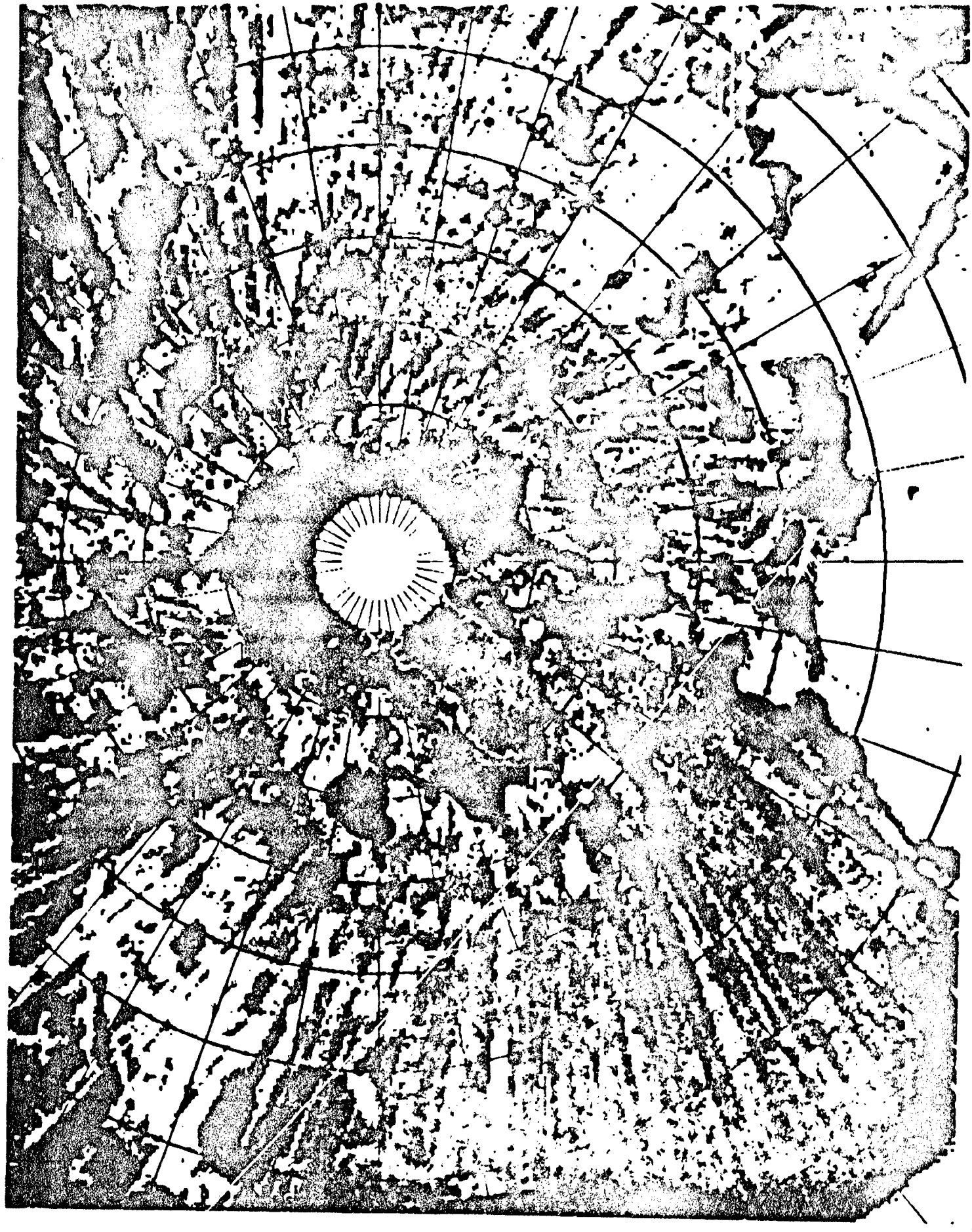

During September and October 1979, we developed formulae and software to produce a new gain state profile to increase uniformly the dynamic range of the sensor throughout the orbital track. The dynamic range was increased by 7.2 dB in late October 1979, raising the threshold for sensor saturation from 23% to 53% reflectivity. Further changes were not possible for areas within 40.7 degrees of the sub-solar point by virtue of sensor design limitations. Unfortunately, most of the highly reflective features fell within those areas. We soon found that the increased dynamic range did not completely eliminate the saturation problem.

To isolate areas of persistent high reflectivity, we prepared a SSC minimum brightness data base using data acquired on the following days:

31 Oct 1979;
1, 2, 3, 13, 14, 15, 16, 20, 21 and 30 Nov 1979;
1, 2, 5, 6, 7, 8, 9, 12, 13, 14, 15, 16 and 17 Dec 1979.

We displayed this data base in transparency format (Figure 3.2) and noticed that arid areas, such as the Sahara, had reflectivities greater than 53%. We also noticed when comparing raw L-detector data with SSC data, that some liquid water clouds also had apparent reflectivities greater than 53%. At that point we ruled out worldwide use of the SSC detector as a "stand-alone" cloud detection device. We concentrated on developing a multi-spectral algorithm which would use SSC data in conjunction with DMSP OLS data to make cloud/no cloud and snow/no snow decisions.

We prepared statistical analyses of SSC minimum brightness within several areas, land only, scattered throughout the Northern Hemisphere (Figure 3.3). We eliminated every point north of 69°N from consideration because, by the end of the period, all of those points were either in twilight or in total darkness. We found that areas containing persistent snow cover had reflectivities, in the near-IR, between 6 and 13%. We also matched the minimum brightness display (Figure 3.2) with weekly Snow and Ice Boundary Charts (Figures 3.4 thru 3.8) prepared by NOAA/NESS. Notice the excellent agreement between an area of bright snow in the mid-western part of the United States (Figure 3.6) and a similar area of low near-IR reflectivity in the SSC minimum brightness display (Figure 3.2). These comparisons suggest that low near-IR reflectivites alone are an excellent indicator of snow cover. This conclusion, however, is not valid over water where water and ice reflectivities are comparable.

Our next task centered on developing an understanding of the functional relationship between SSC and primary detectors (both L and T) responses over cloud, cloud-free, and snow covered scenes. We developed software to compute the average L- and T-detector responses within the IFOV of each SSC detector. We analyzed 21 quarter orbits (16 N. Hemisphere; 5 S. Hemisphere) of SSC, L-detector, and T-detector data and concluded:

Thick cirrus clouds reflect from 13% to 26% of incident solar energy in the SSC spectral band.

Figure 3.2. A display of SSC minimum brightness (next page) based on SSC data collected during October, November, and December 1979. Brightness is represented by 16 greyshade values ranging from black to white. The sensor was set to produce full- scale output whenever scene reflectances exceeded approximately 53%. The white disk at the pole is merely a data void area. Notice that semi-arid and arid features caused full-scale output. However, the spatial extent of this output is much less than before (Figure 3.1). The dark areas over land have reflectivities roughly equal to the reflectivity of snow in the near-infrared portion of the spectrum (Valovcin (1978)). In fact, these areas represent the spatial extent of the Northern Hemisphere snow cover exceptionally well (Figures 3.4 through 3.8).

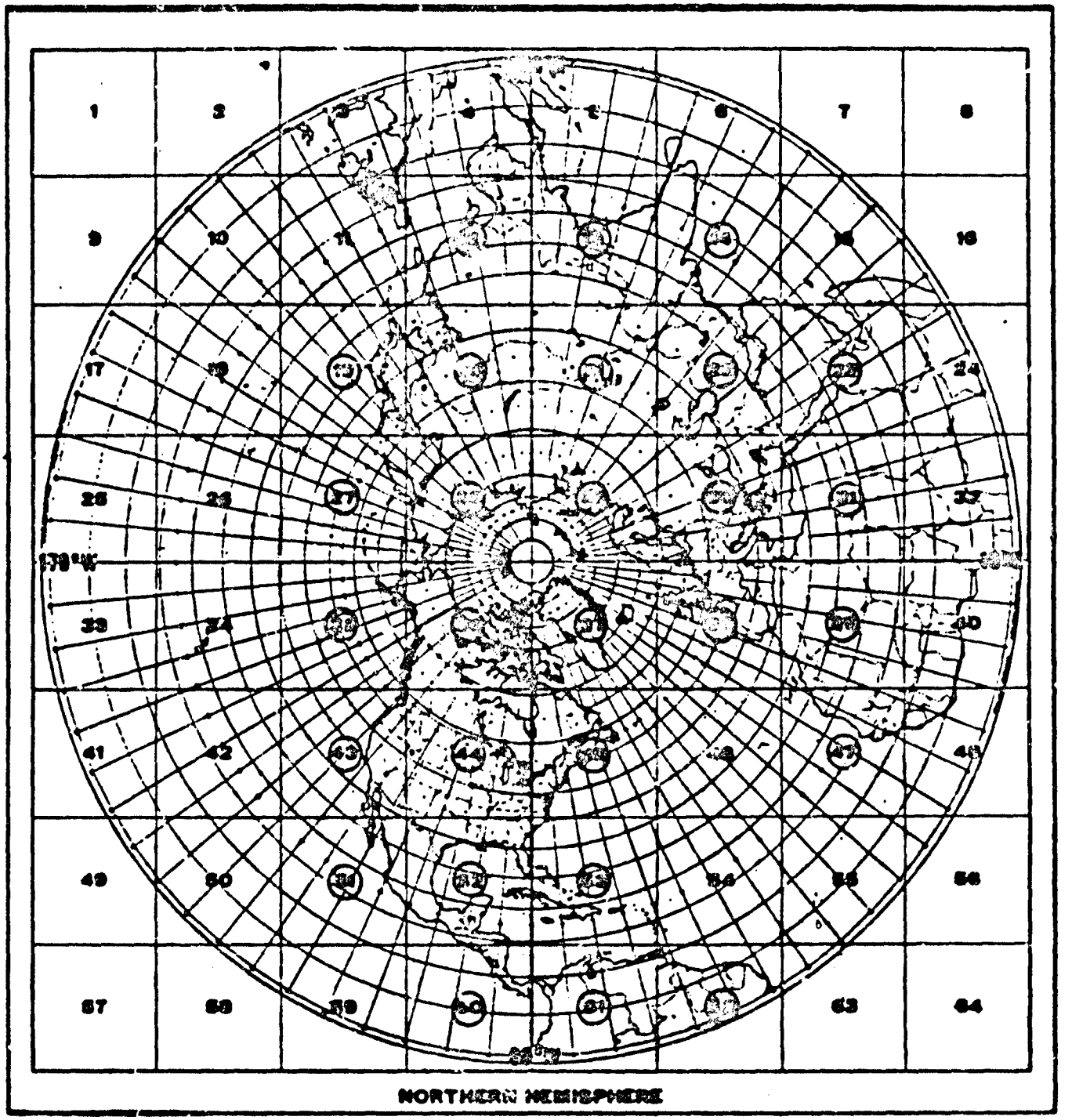

Figure 3.3. Statistical analyses of SSC minimum brightness were prepared within the areas containing circled numbers.

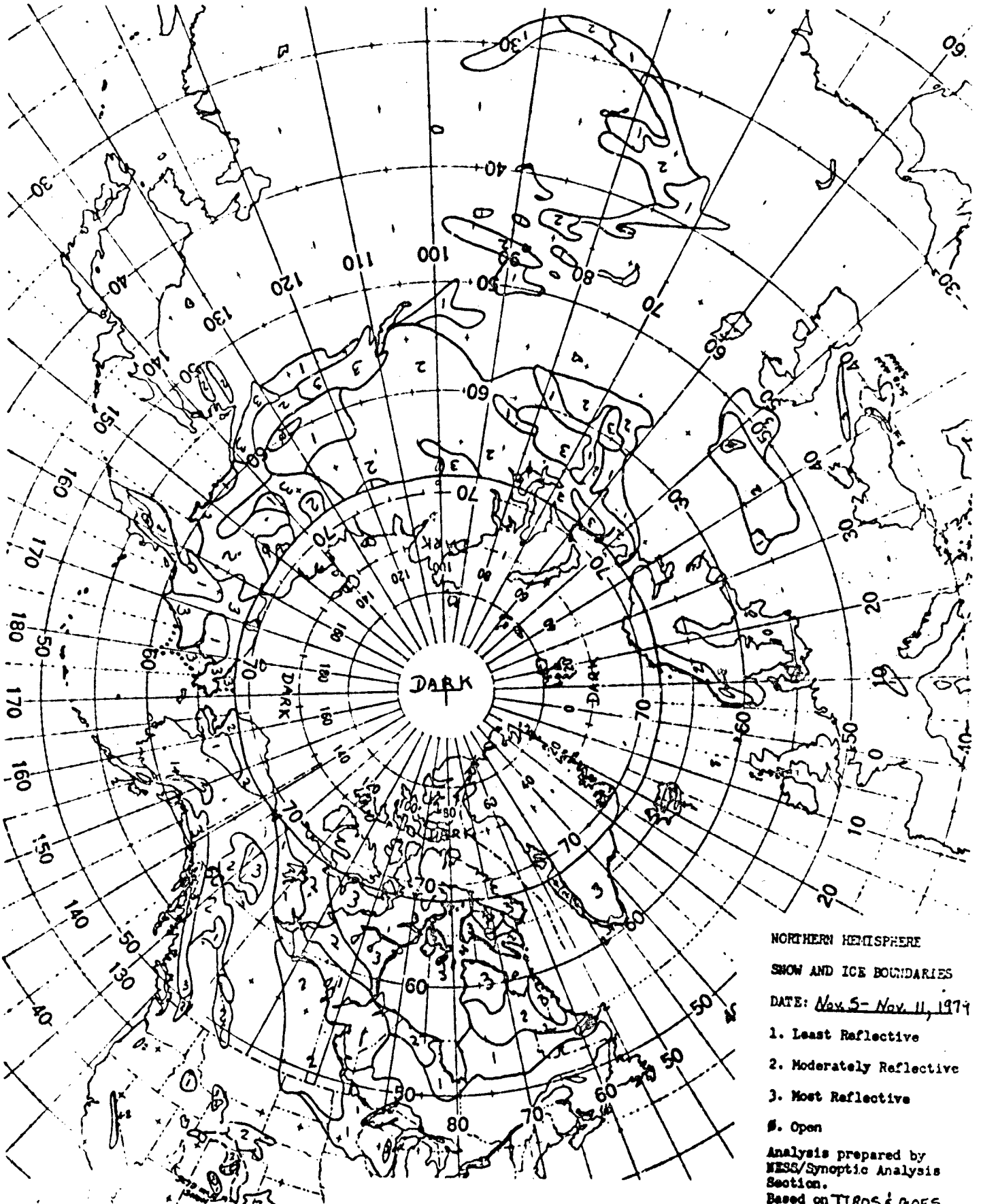

Figure 3.4. Snow cover chart.

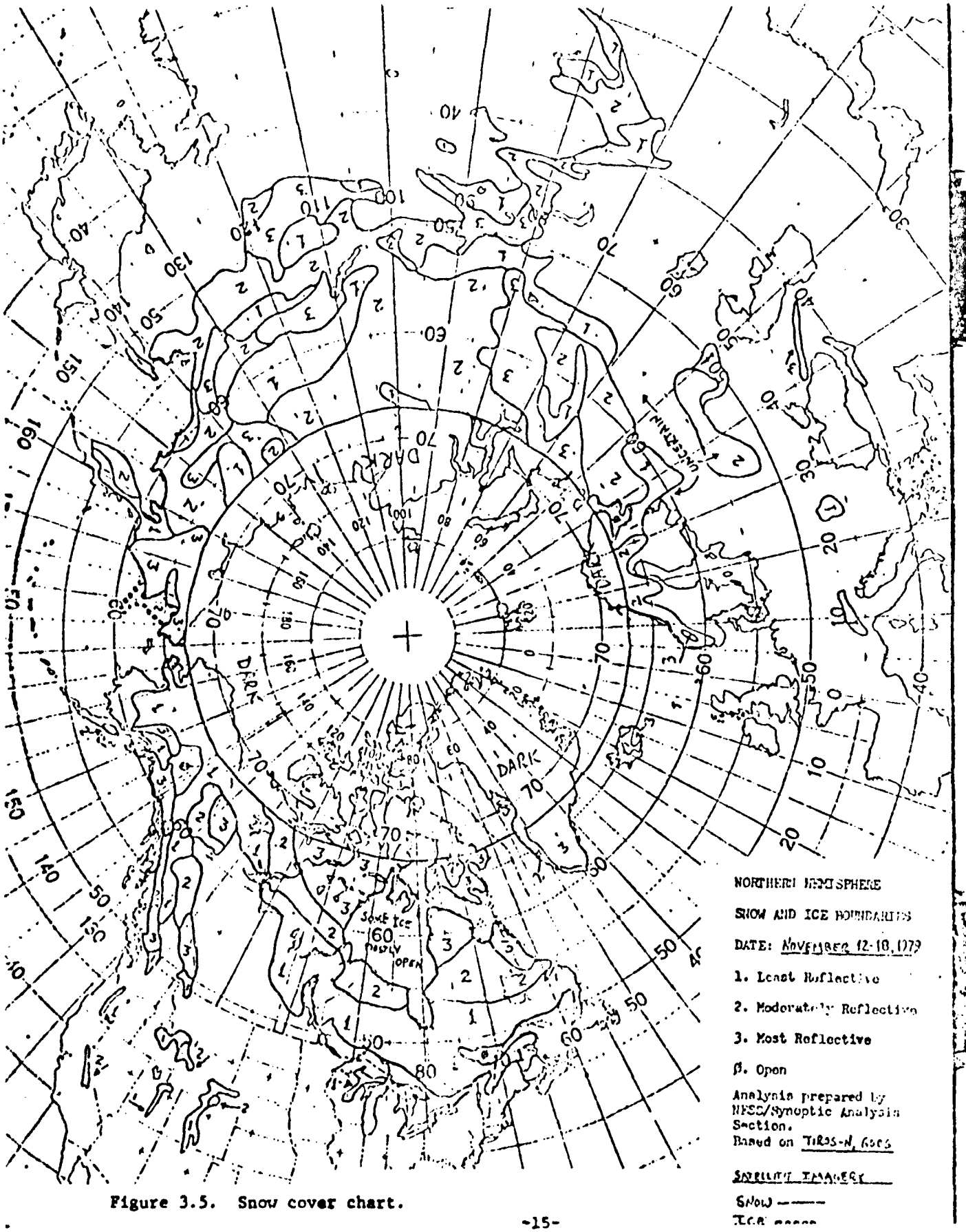

Figure 3.5. Snow cover chart.

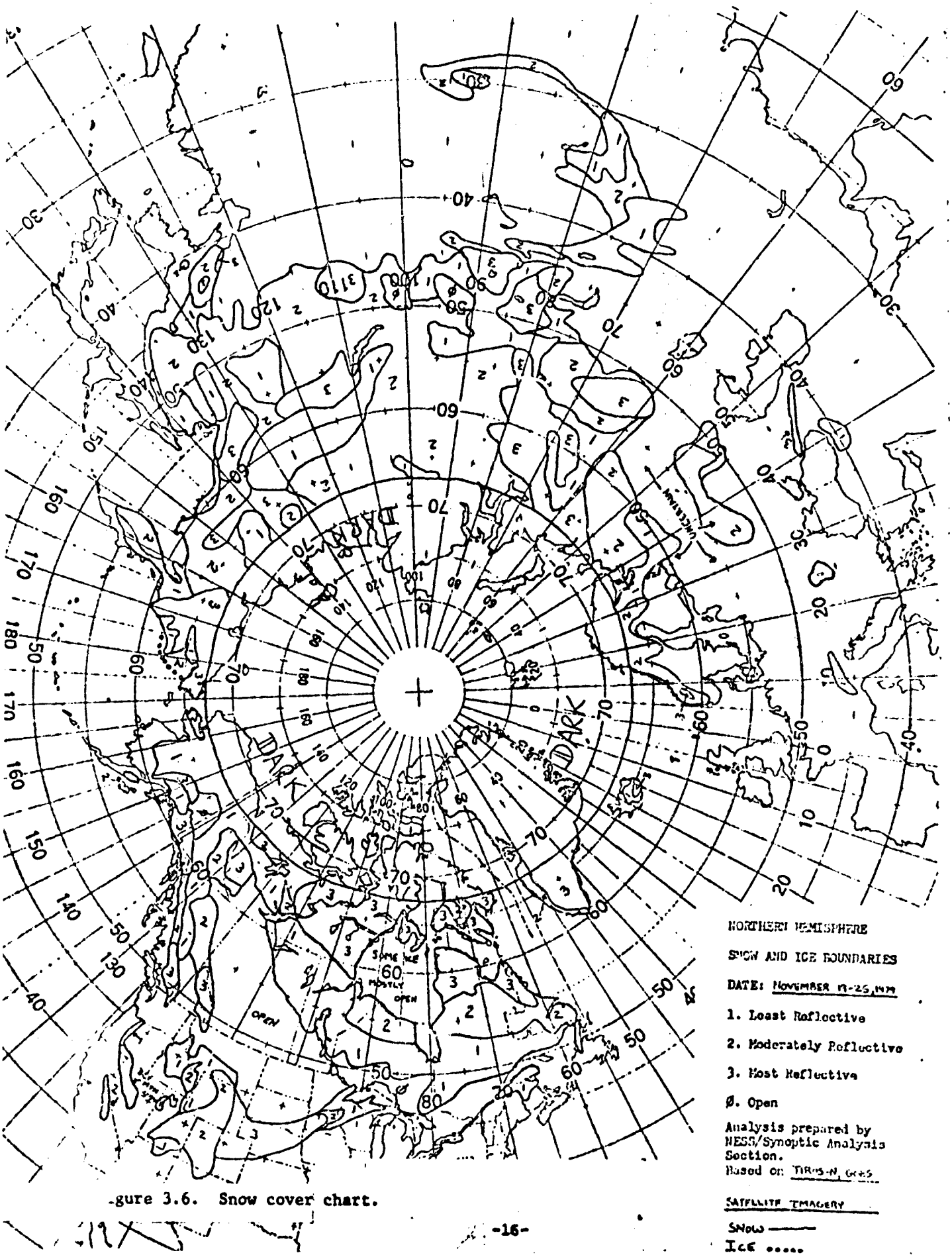

Figure 3.6. Snow cover chart.

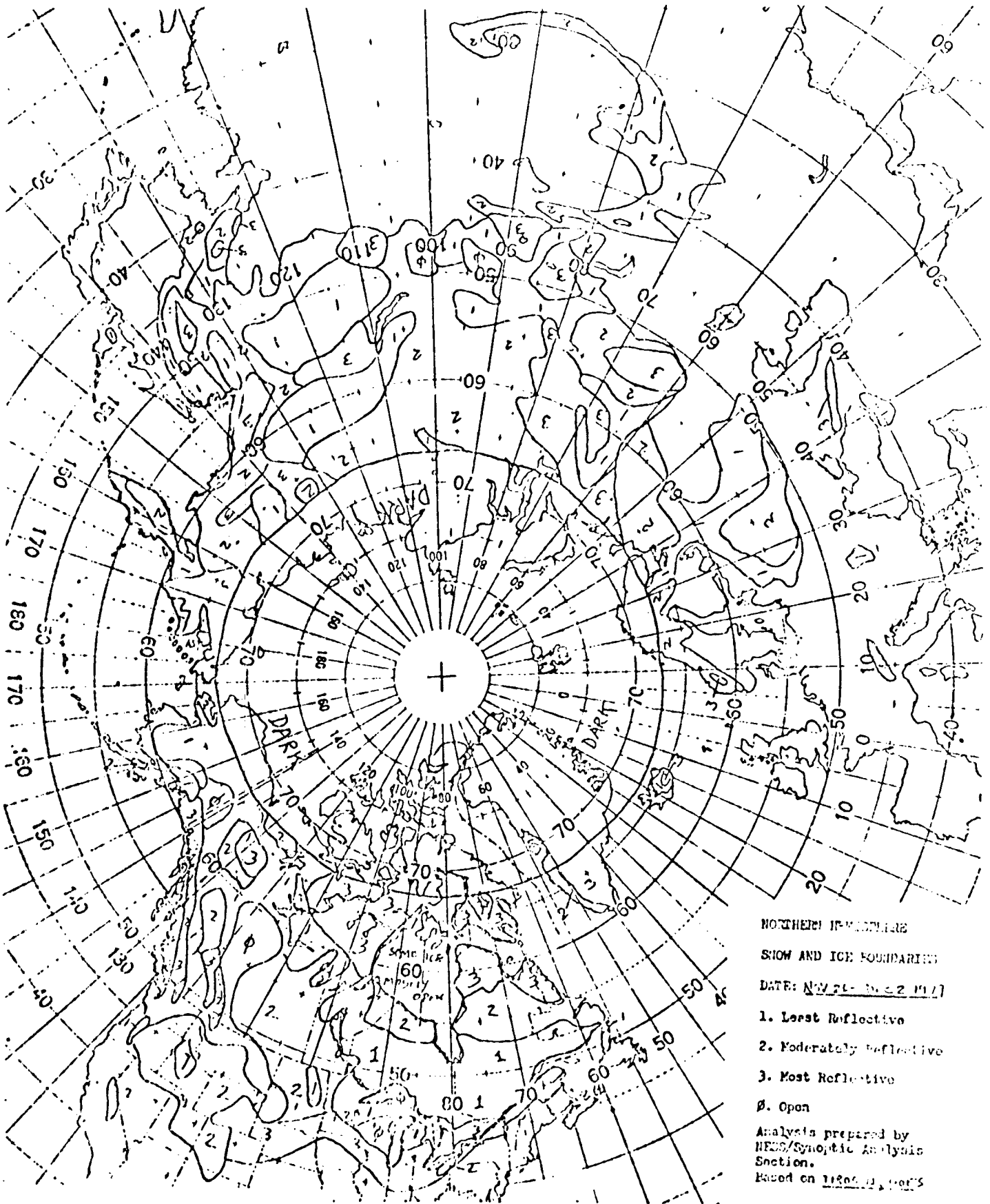

Figure 3.7. Snow cover chart.

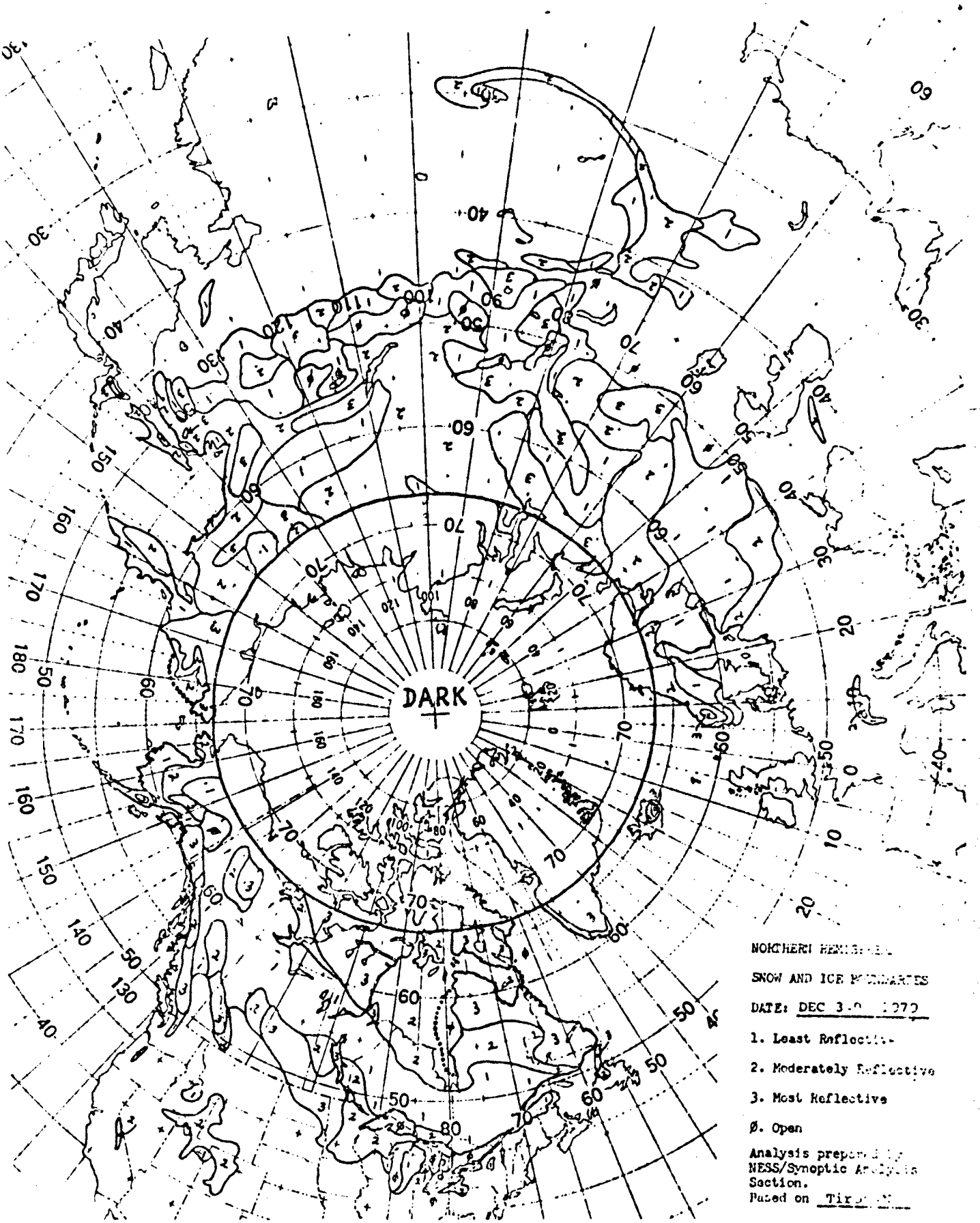

Figure 3.8. Snow cover chart.

Clear ocean scenes reflect from 1 to 2% of incident solar energy in the SSC spectral band.

Liquid water clouds reflect, in most cases, more than 53% of incident solar energy in the SSC spectral band.

The SSC response is directly proportional to L-detector response over clear, snow-free features.

We still needed to develop a functional relationship between SSC and L-detector responses from snow (ice) and cloud-filled scenes. We planned to use 3DNEPH and SNODEP models for cloud and snow depth information, respectively, to separate matching SSC, L-detector, and T-detector samples into cloud-free, snow-filled, and cloud-covered categories. We then planned to prepare scatter diagrams of SSC versus both L- and T-detector responses for each of these categories and to develop the required multi-spectral processing algorithm. Furthermore, we planned to test the performance of the algorithm against independent sets of merged L-detector, T-detector, and the SSC data and compute the statistical reliability of the multi-spectral processing technique. However, the sudden deactivation of the SSC on 29 December 1979 and subsequent cessation of all planned SSC testing forced us to revise our plans. This revision was begun by reviewing the quality of the 3DNEPH and SNODEP analyses which were on hand. Until that time, we had been quality controlling and correcting deficiencies in 3DNEPH analyses of F4 data only to meet operational requirements. Also, most of the saved L- and T-detector data covered the eastern portion of North America where snow cover was generally restricted to remote areas of Canada and conventional observations of snow depth were very sparse. Consequently, the SNODEP model relied almost exclusively on climatology as a source of snow depth information. As a result the SNODEP analyses in those areas were not as reliable as we would have liked them to be. Therefore, we decided to use manually prepared verification data bases in lieu of the 3DNEPH and SNODEP analyses.

We manually produced a verification data base using transparencies of SSC and matching L- and T-detector data. We selected the following four quarter orbits of L-detector, T-detector, and SSC data for verification:

Data revolution 2552 on 3 Dec 1979 over North America (Figure 3.9).

Data revolution 2680 on 12 Dec 1979 over North America (Figure 3.10).

Data revolution 2680 on 12 Dec 1979 over Antarctica (Figure 3.11).

Data revolution 2860 on 25 Dec 1979 over Eurasia (Figure 3.12).

We took the following steps to prepare the verification data:

We prepared transparencies of the L- and T- detector data which included timing marks every 2 seconds.

We adjusted SSC data to compensate for solar zenith angle and actual gain state thereby normalizing sensor response to 0^{o} solar zenith angle.

Figure 3.9. A display of matching DMSP visual (3.0nm resolution) and SSC imagery (next page), left and right respectively. These data were collected over North America on 3 December 1979 during orbital revolution 2552. In the SSC display, clouds are much brighter than clear, snow-covered terrain. However, liquid water clouds are brighter than cirrus clouds in the SSC imagery. Cloud-free water scenes appear dark in both displays. The black vertical lines in the SSC imagery represent gaps in the SSC data in the cross-track direction (Figure 2.2). The image processing technique has removed some of these gaps.

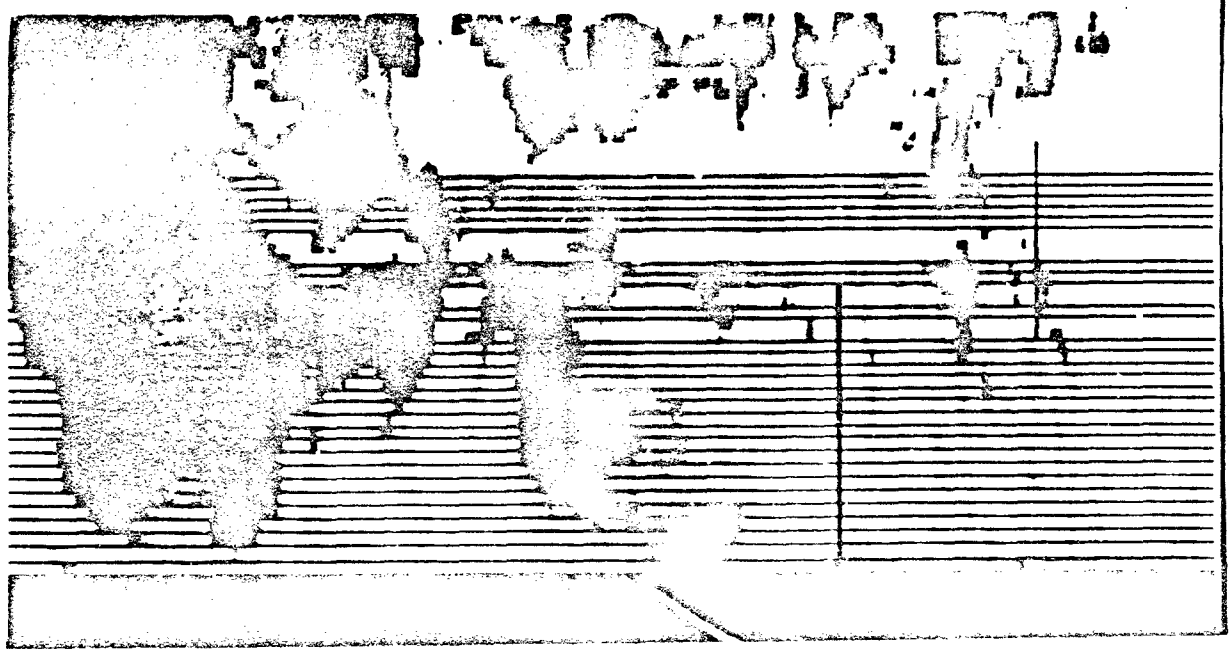

Figure 3.10. A display of matching DMSP visual (3.0nm resolution) and SSC data (next page), left and right respectively. These data were collected over North America on 12 December 1979 during orbital revolution 2680. Areas of clear, snow-covered terrain can be found in the center-left portion of the visual imagery. The snow has roughly the same brightness as nearby cloud cover. The snow is much darker, however, than the clouds in the SSC display, making snow/cloud discrimination easier with the SSC imagery than with visual data. The upper portion of the SSC imagery (i.e., the white area) did not receive sufficient daylight to permit image processing. All but the upper portion of the display was used in preparing a verification data base.

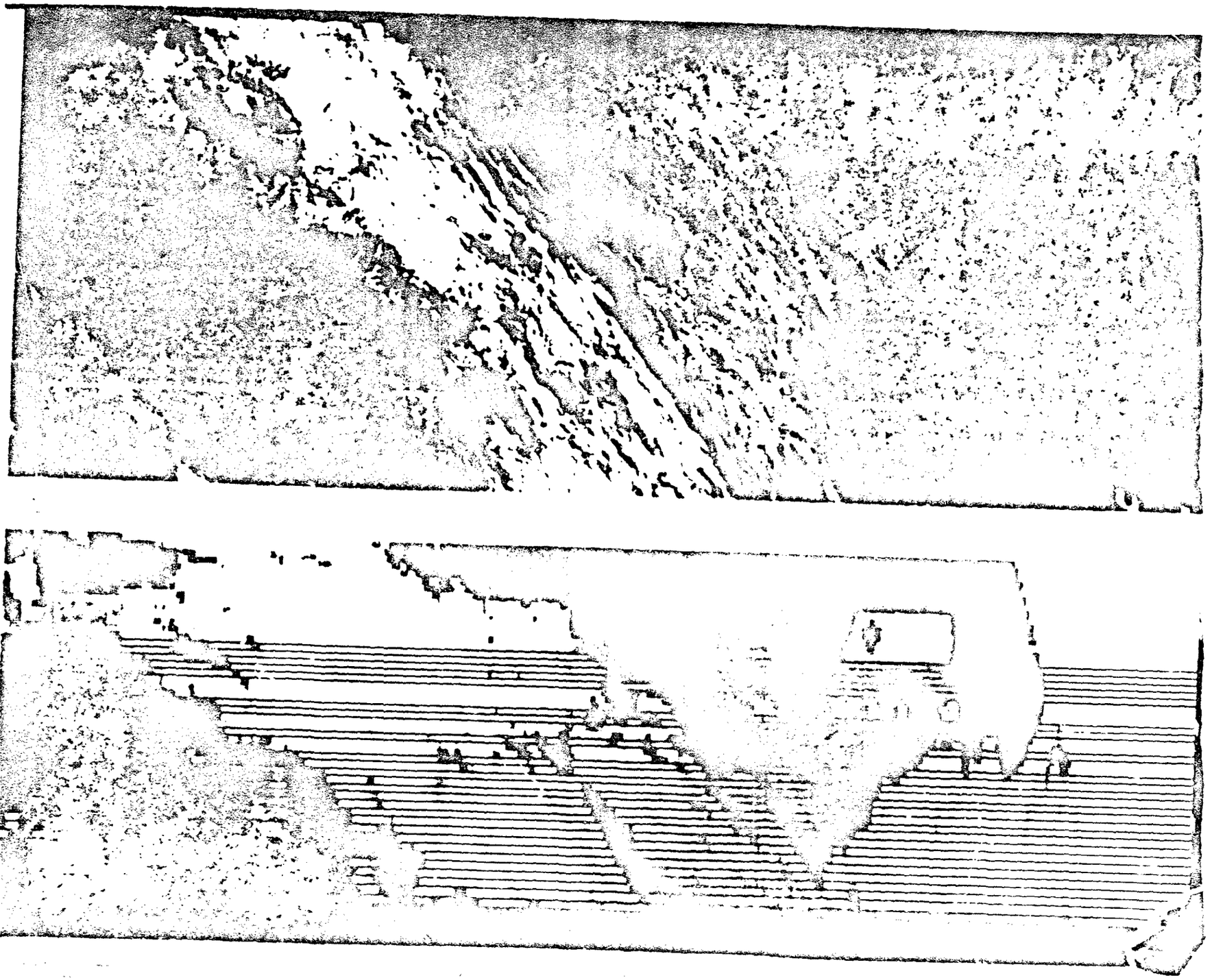

Figure 3.11. A display of matching DMSP visual (3.0nm resolution) and SSC data (next page), left and right respectively. These data were collected over Antarctica on 12 December 1979 during orbital revolution 2680. Notice the excellent contrast between bright clouds and dark snow in the SSC display compared to the relatively poor contrast between bright snow and clouds in the visual imagery.

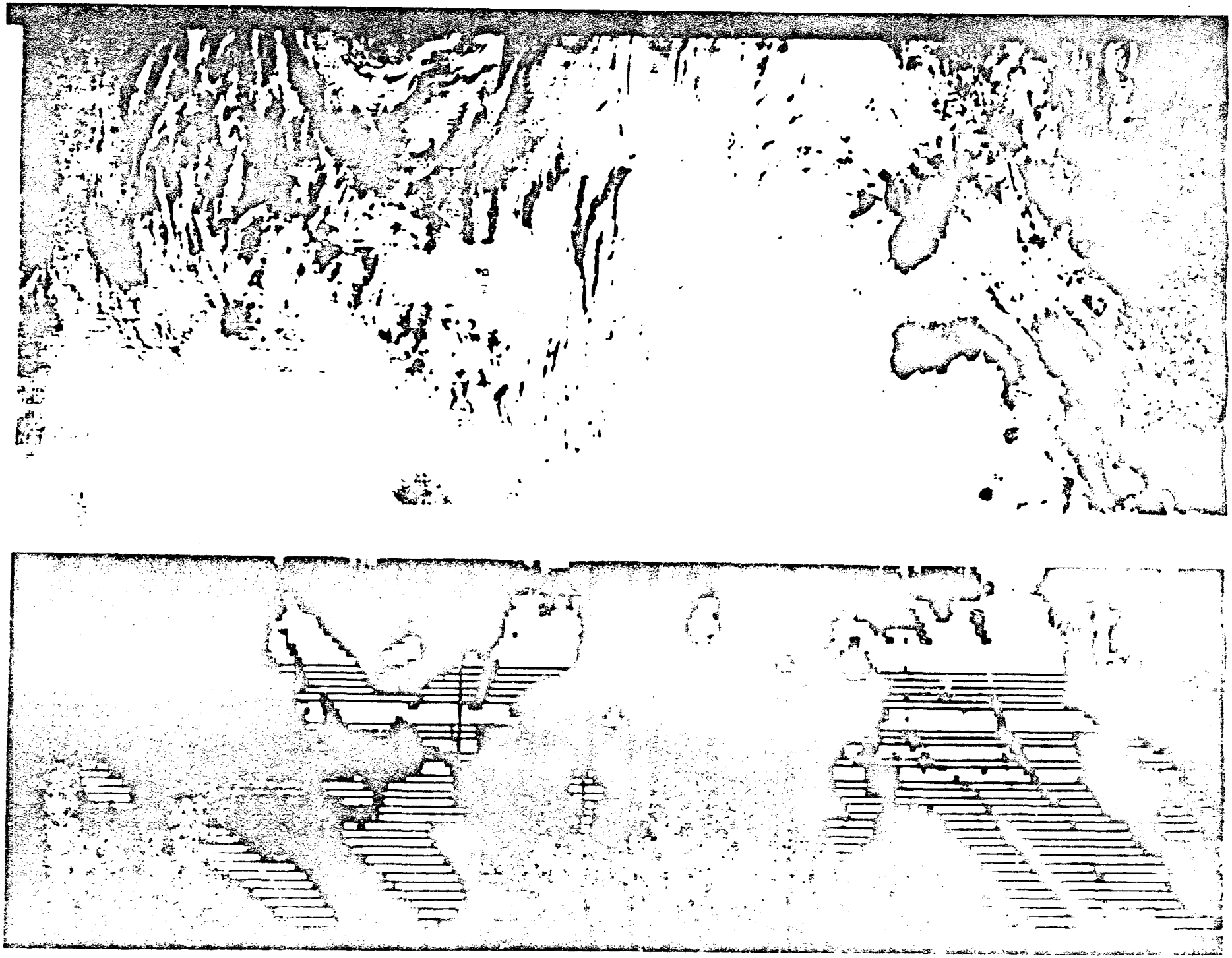

Figure 3.12. A display of matching DMSP visual (3.0nm resolution) and SSC data (next page), left and right respectively. These data were collected over Eurasia on 25 December 1979 during orbital revolution 2860. A narrow band of status clouds is located in the upper quarter of the visual imagery. Next to these clouds is an area of clear, snow-covered terrain. DMSP thermal data (not shown) indicate that the cloud top temperature is warmer than the adjoining snow-covered terrain. Current 3DNEPH satellite data processing techniques would have failed to detect these clouds. Notice, however, how well these clouds stand out against the dark snow background in the SSC display. Cirrus clouds are less bright than liquid water clouds in the SSC imagery. The lower portion of the images cover part of the Middle East. Notice that clear, arid terrain features caused full-scale output of the SSC sensor.

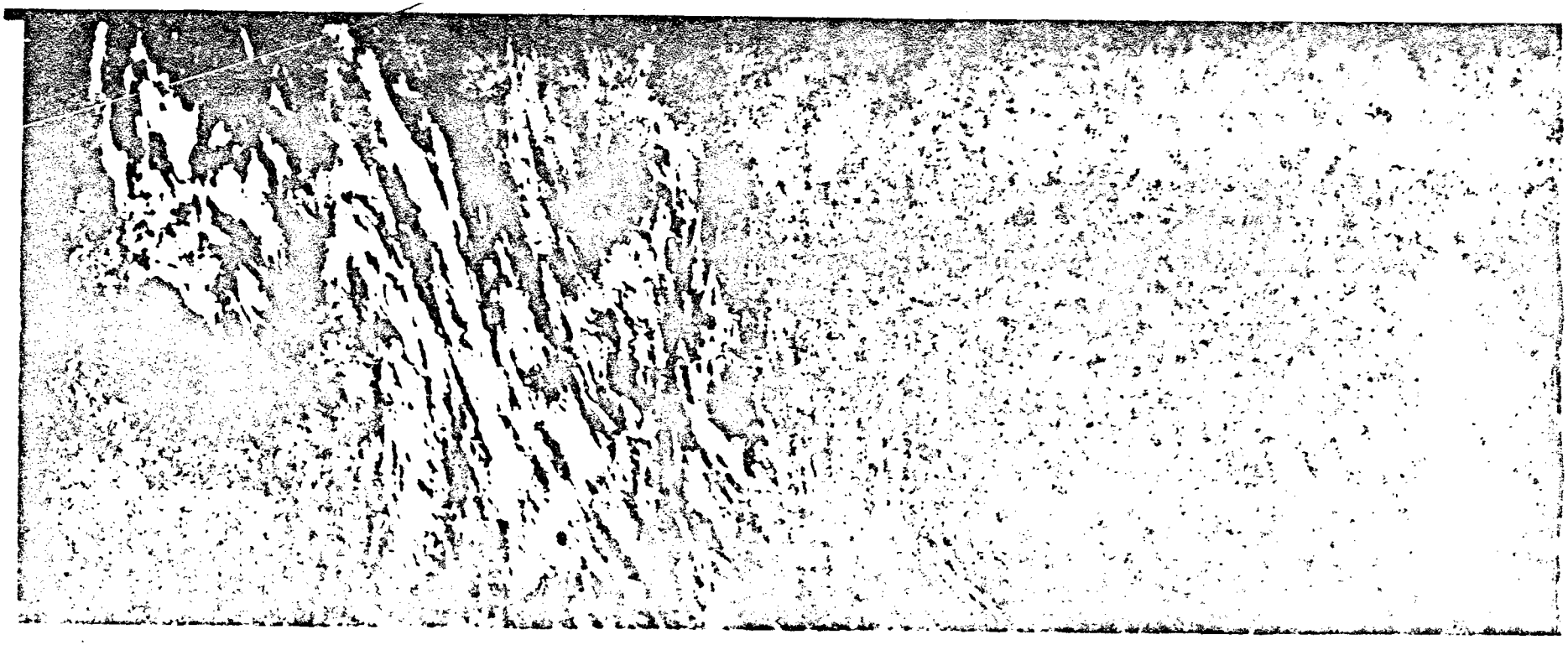

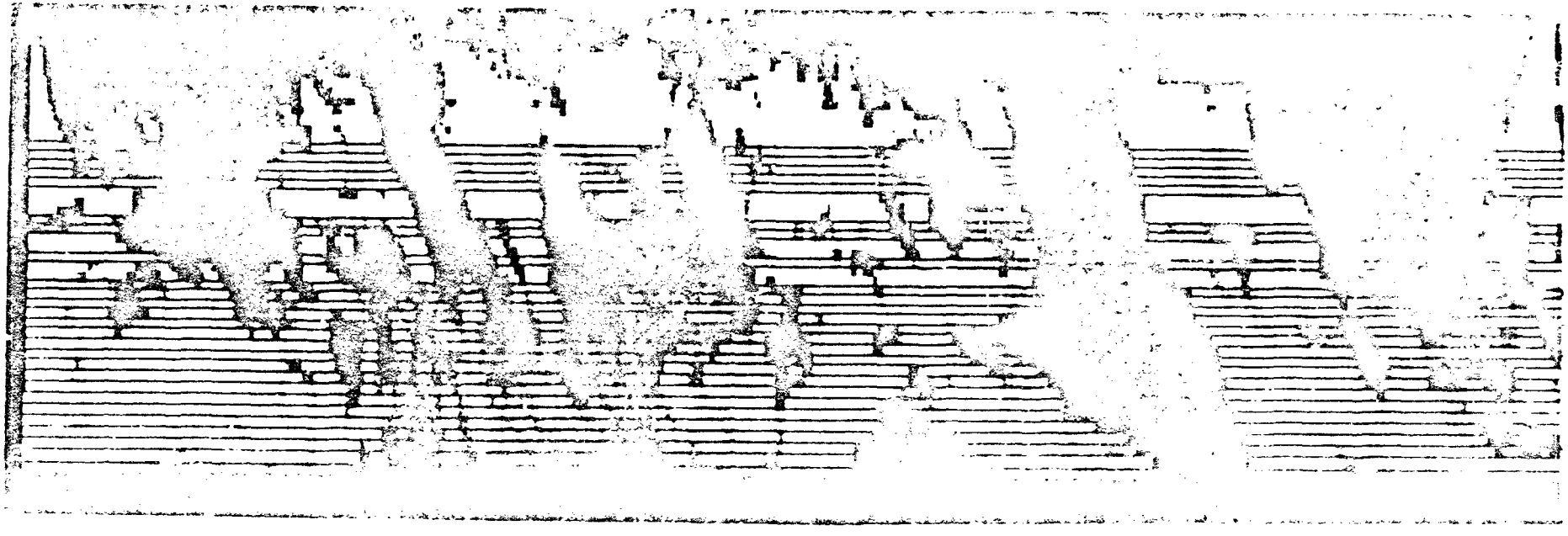

We mapped SSC data into an L- and T-detector format and displayed the results on transparencies.

We prepared a template of the IFOV of the SSC detector display at nominal altitude to match L- and T-detector displays.

We placed the template over the L- and T-detector displays at time marks corresponding to known SSC data times.

We inspected all available data and decided whether there was snow, cloud, or no cloud within the IFOV of each SSC display. We treated any amount of cloud within the IFOV, even a single L- or T-detector pixel, as a cloudy SSC pixel. Similarly, any amount of snow within a clear IFOV was deemed a snow-filled pixel. In other words, we made no provision for partly cloudy scenes, or, for that matter, mixed snow and non-snow scenes. Mixed snow and cloud scenes were treated as cloudy scenes.

We used these results to stratify the merged data sets into clear, cloudy, and snow (ice) categories.

We then prepared scatter diagrams of responses from coincident SSC and average L-detector samples and coincident SSC and average T-detector samples within each of the categories (Figures 3.13 through 3.18).

Analysis of these diagrams showed the best potential for snow, cloud, and cloud-free scene discrimination could be achieved by interpreting coincident average L-detector and SSC samples. Figure 3.13 reinforced our previous conclusion that cloud-free SSC response is directly proportional to coincident average L-detector response. Comparison of Figure 3.13 with Figure 3.15 showed excellent separation between clusters of points of SSC versus average L-detector samples acquired over cloud-free and snow-covered scenes. Detailed analysis of the data in Figures 3.13, 3.15, and 3.17 showed that clusters of points of SSC versus average L-detector samples acquired over clouds were generally located away from the clusters of clear and snow-filled points. However, a limited amount of cloud samples overlap slightly into the scatter of both snow and cloud-free samples. We formed a composite diagram of all samples and divided the matrix of possible combinations of SSC versus average L-detector responses into cloud, snow (ice), and cloud-free regions to minimize the overlap (Figure 3.19). The matrix provided a mechanism for making unique cloud, snow, or cloud-free decisions based merely on matching SSC and average L-detector responses. We developed an automated algorithm which effectively uses the matrix as a sample look-up table to determine scene content.

During the final phase of our evaluation, we determined the statistical reliability of this algorithm by comparing results obtained from the algorithm to manually prepared verification results. Tables 3.1 through 3.4 contain results obtained from the algorithm for cloud-free, snow-filled, or cloud-filled categories versus verified results for each of the four selected quarter-orbits of data. Table 3.5 depicts the combined results. Each row

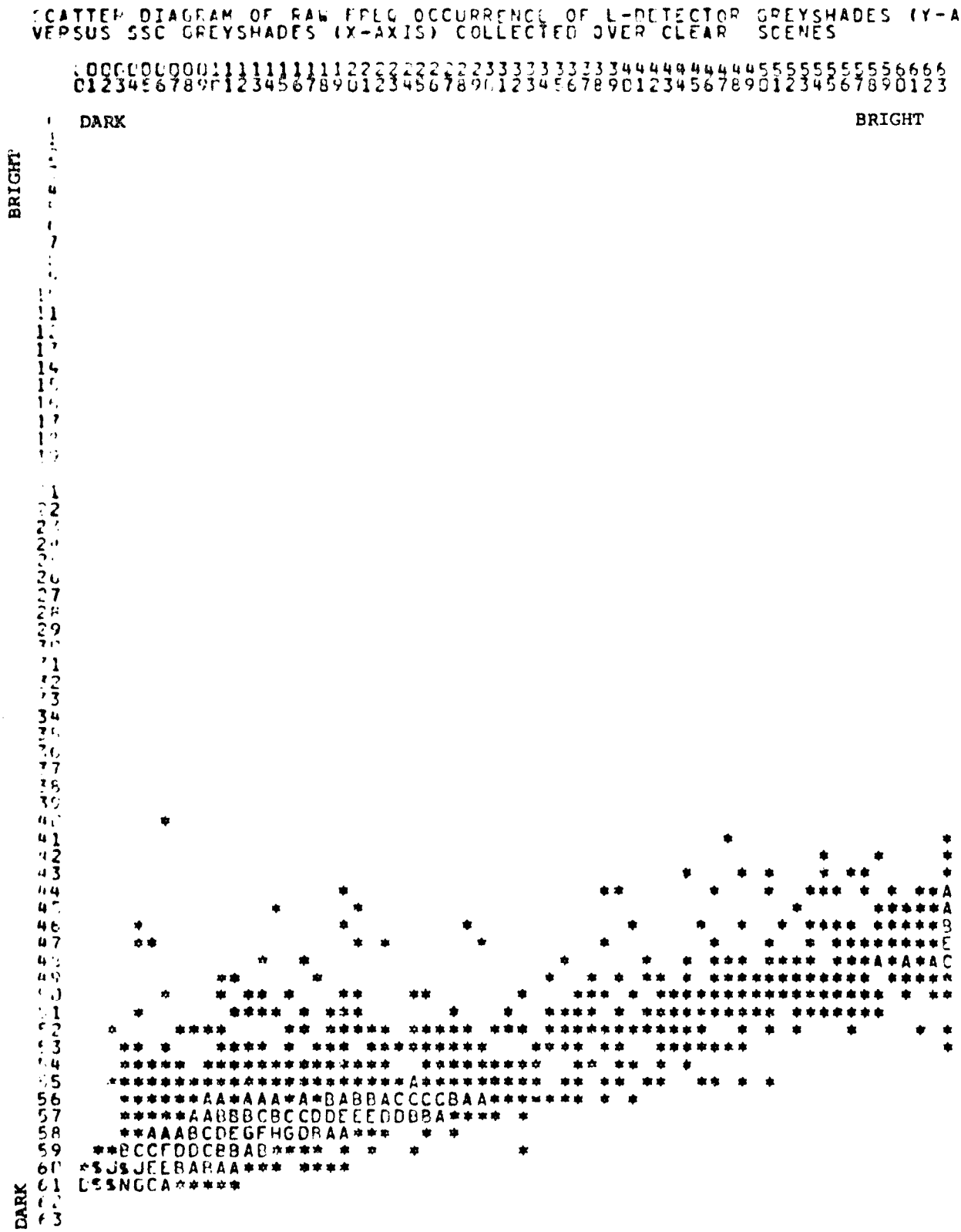

Figure 3.13. Scatter diagram of L-detector and SSC output from clear scenes.

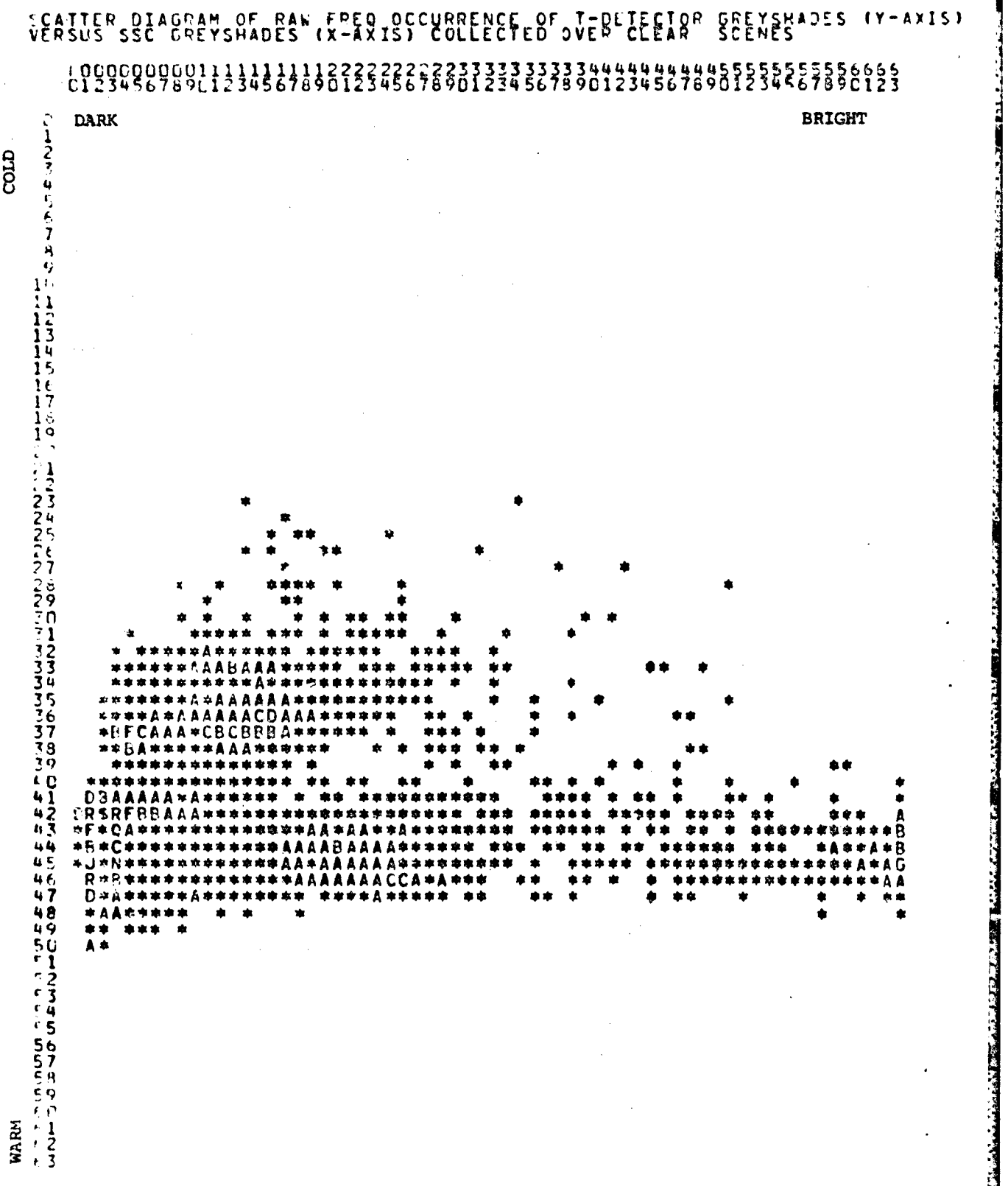

Figure 3.14. Scatter diagram of T-detector and SSC output from clear scenes.

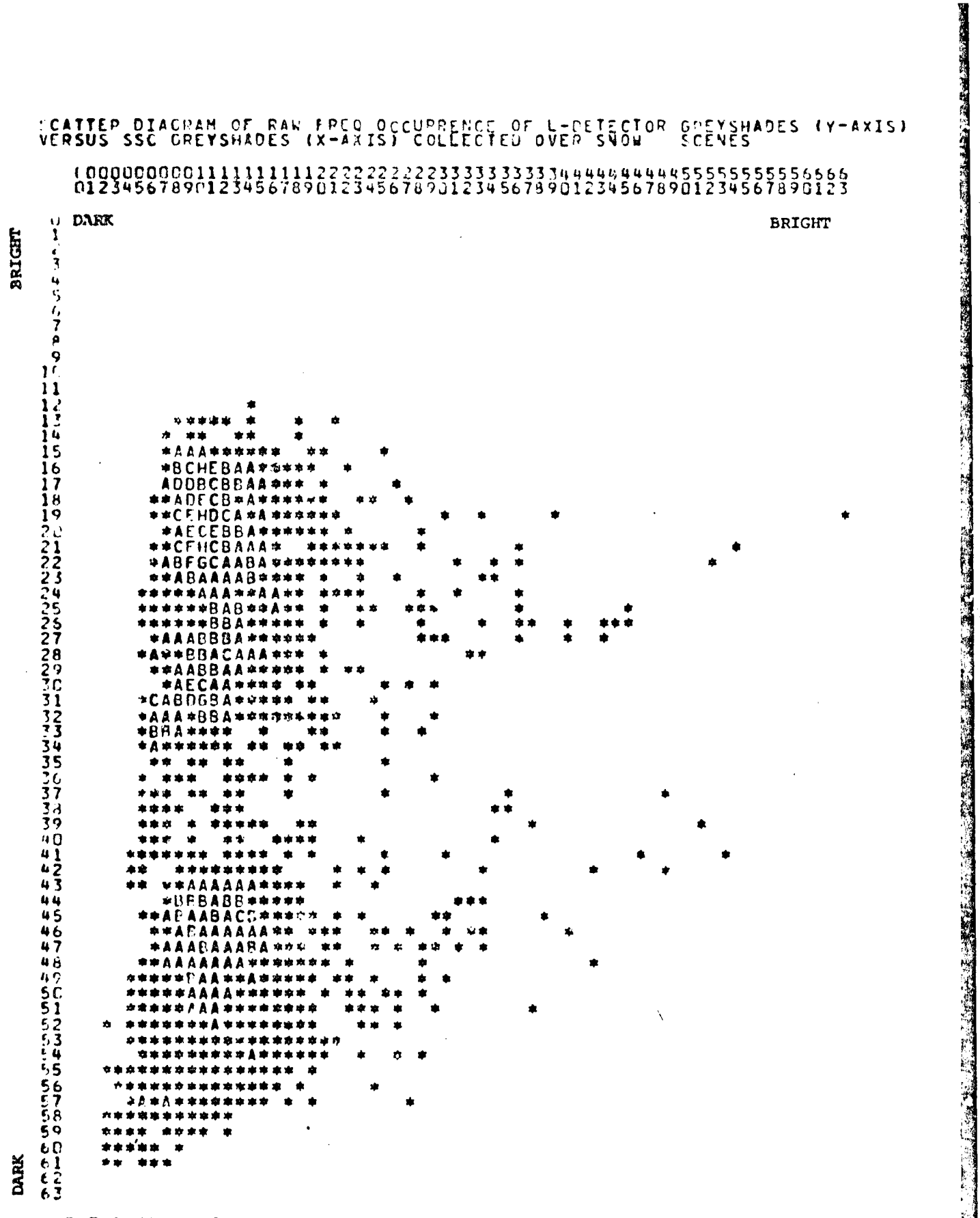

Figure 3.15. Scatter diagram of L-detector and SSC output from snow scenes.

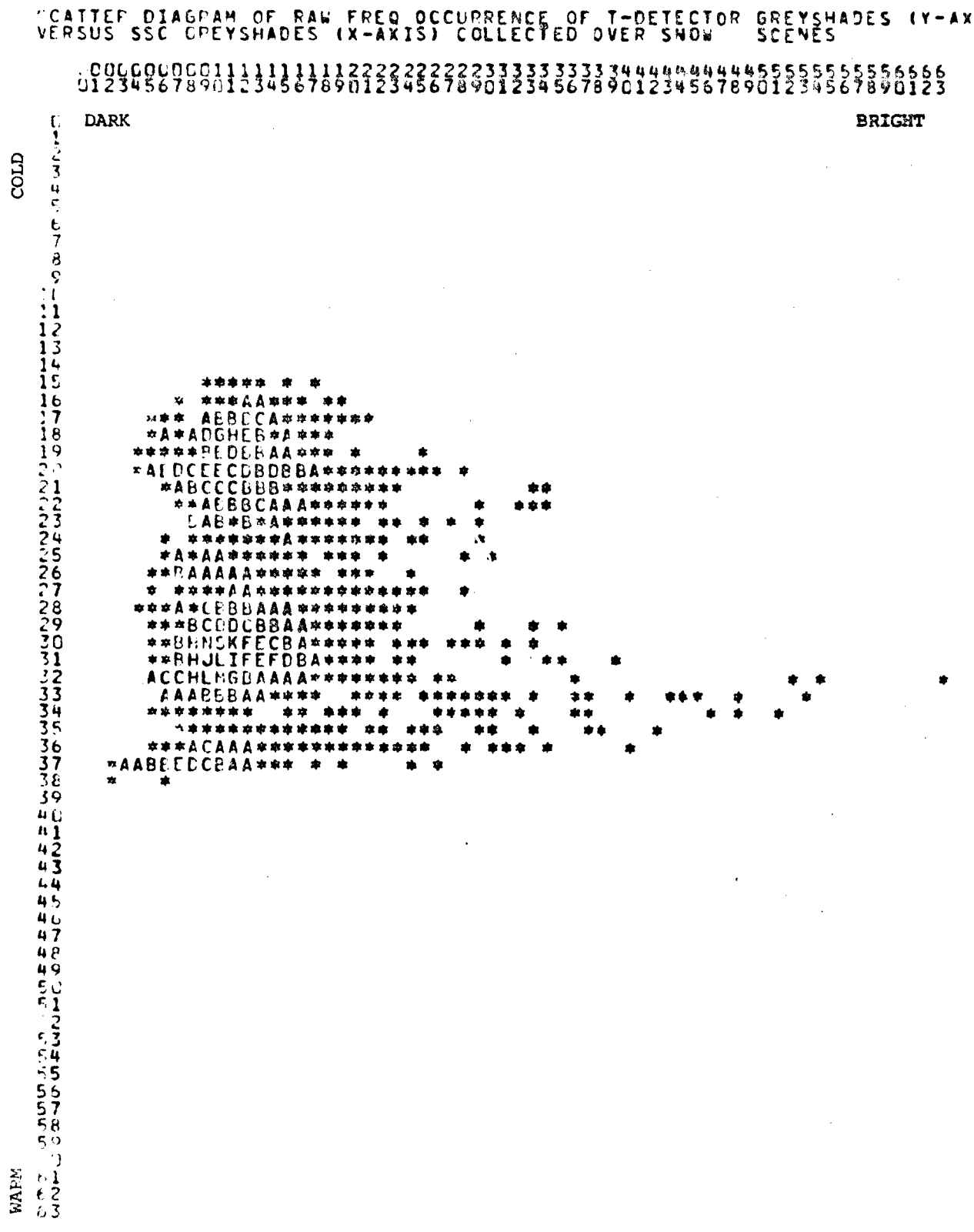

Figure 3.16. Scatter diagram of T-detector and SSC output from snow scenes.

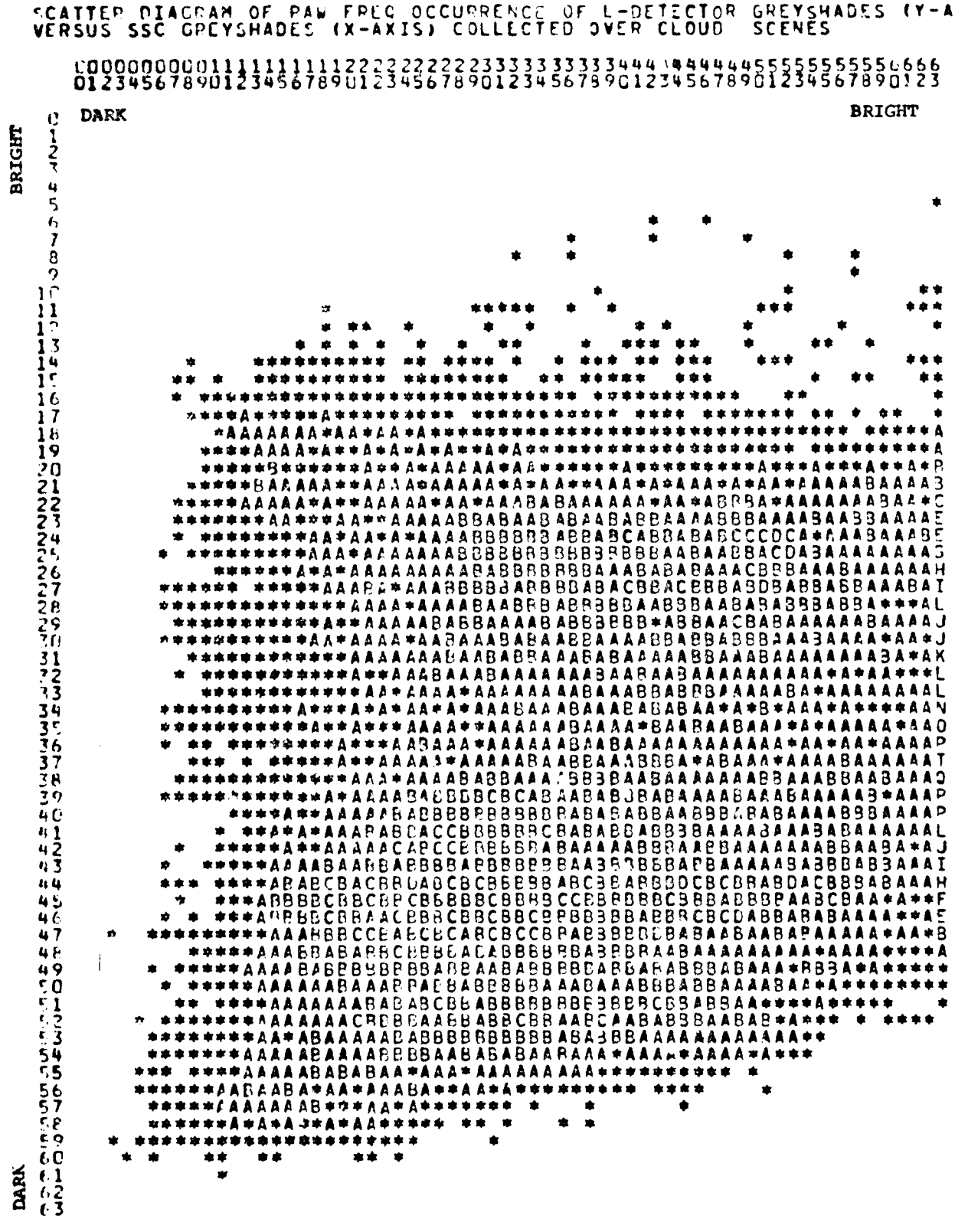

Figure 3.17. Scatter diagram of L-detector and SSC output from cloud scenes.

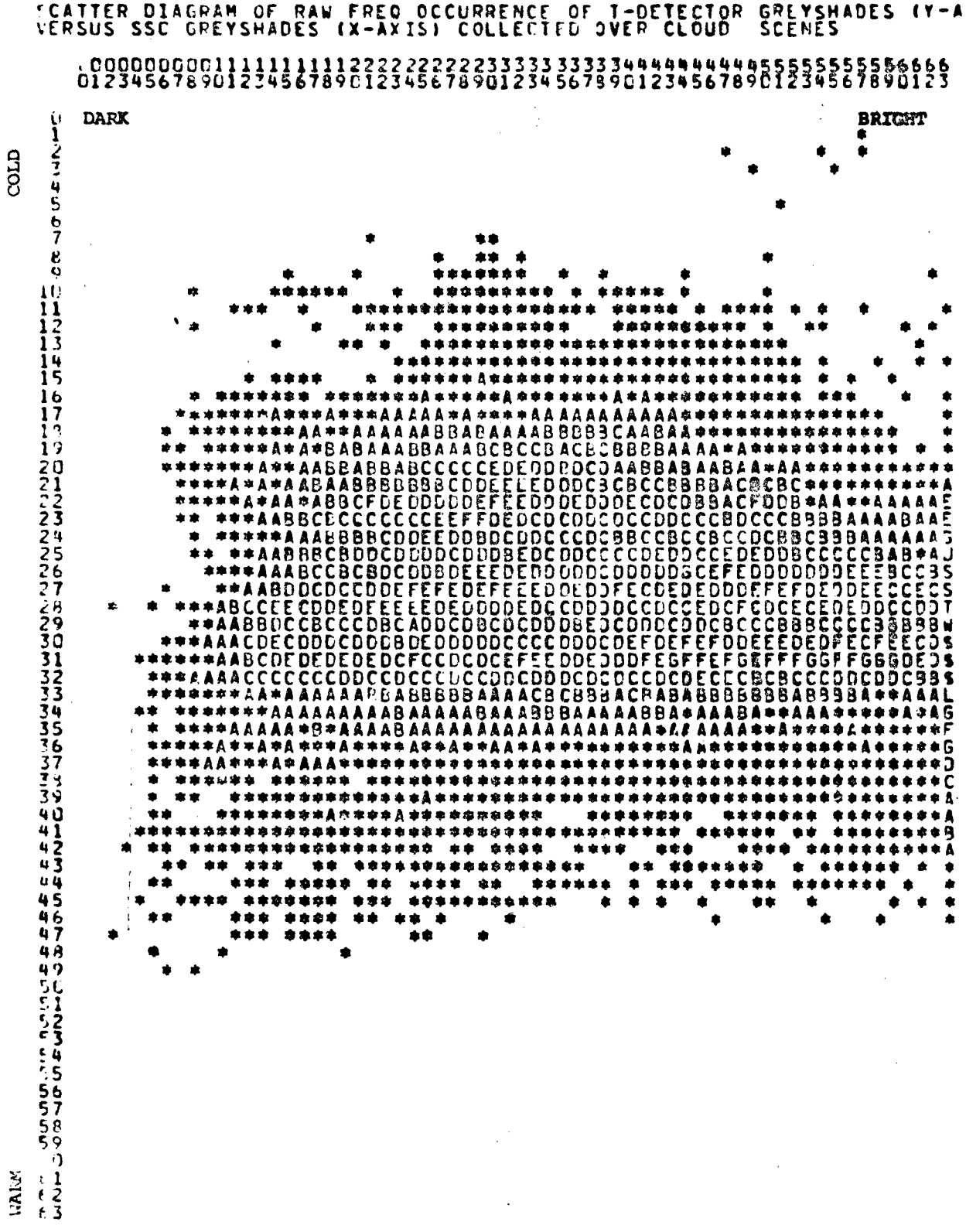

Figure 3.18. Scatter diagram of T-detector and SSC output from cloud scenes.

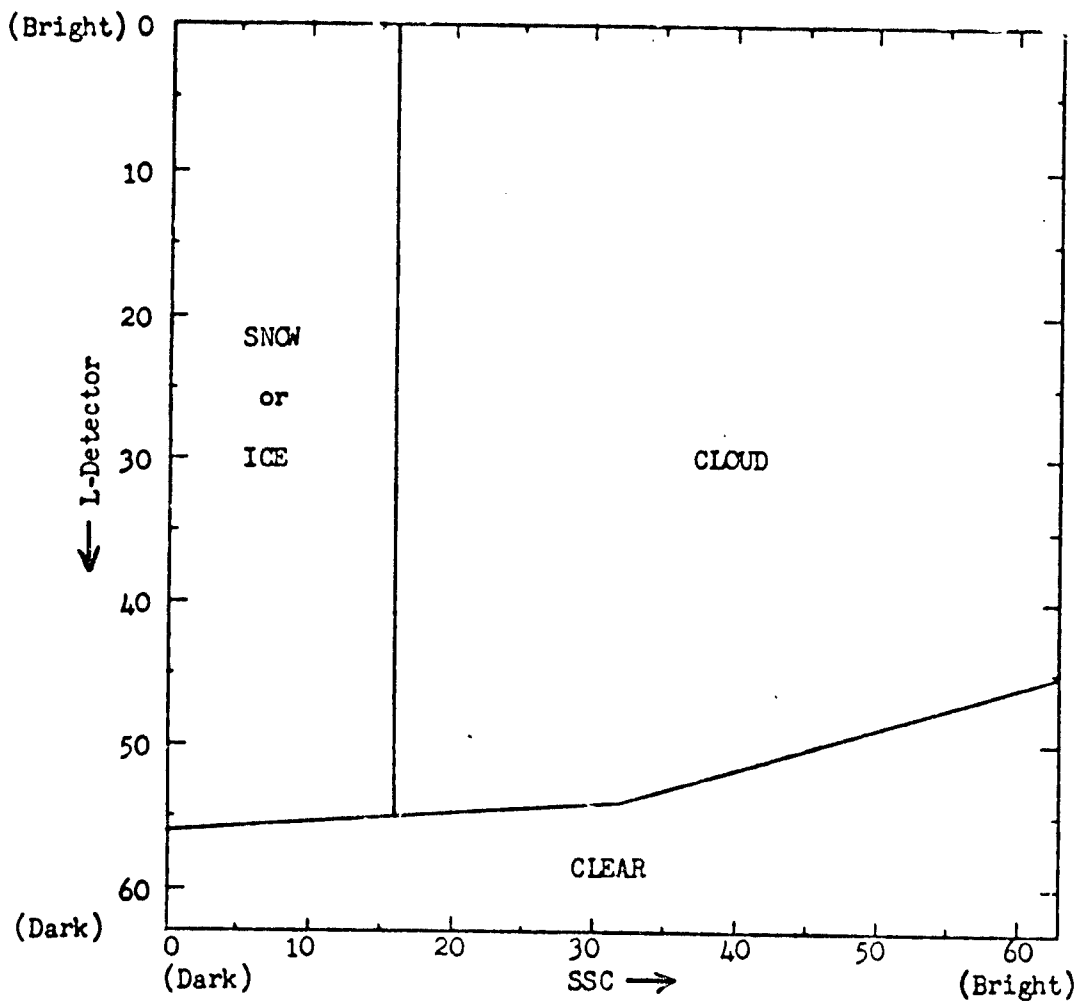

Figure 3.19. Cloud/clear/snow decision matrix.

		MANUAL			
		CLEAR	SNOW	CLOUD	
SSC	CLEAR	95.5%	3.0%	1.5%	(2172)
	SNOW	1.3%	83.0%	15.7%	(159)
	CLOUD	4.7%	4.5%	90.8%	(6405)
		(2375)	(488)	(5873)	(8736)

Reliability of cloud/no cloud decisions = 92.6%

() = Raw frequency

Table 3.1. Verification rates using the decision matrix on data from orbital revolution 2552 and manually prepared analyses as "truth".

		MANUAL			
		CLEAR	SNOW	CLOUD	
SSC	CLEAR	95.9%	0.2%	3.8%	(2294)
	SNOW	0.6%	94.9%	4.8%	(771)
	CLOUD	4.6%	4.6%	90.9%	(8212)
		(2580)	(1114)	(7586)	(11277)

Reliability of cloud/no cloud decisions = 92.3%

() = Raw frequency

Table 3.2. Verification rates using the decision matrix on data from orbital revolution 2680 (North America) and manually prepared analyses as "truth".

		MANUAL			
		CLEAR	SNOW	CLOUD	
S	CLEAR	69.3%	0.2%	30.6%	(528)
S	SNOW	26.2%	67.7%	6.1%	(660)
C	CLOUD	7.0%	4.3%	88.7%	(11240)
		(1395)	(930)	(10203)	(12528)

Reliability of cloud/no cloud decisions = 88.0%

() = Raw frequency

Table 3.3. Verification rates using the decision matrix on data from orbital revolution 2860 and manually prepared analyses as "truth".

		MANUAL			
		CLEAR	SNOW	CLOUD	
S	CLEAR	91.8%	0.0%	8.2%	(207)
S	SNOW	9.9%	81.7%	8.4%	(4140)
C	CLOUD	1.7%	10.9%	87.4%	(8927)
		(750)	(4358)	(8166)	(13274)

Reliability of cloud/no cloud decisions = 88.8%

() = Raw frequency

Table 3.4. Verification rates using the decision matrix on data from orbital revolution 2680 (Antarctica) and manually prepared analyses as "truth".

		MANUAL			
		CLEAR	SNOW	CLOUD	
S	CLEAR	92.4%	1.3%	6.3%	(5301)
S	SNOW	10.3%	81.9%	7.8%	(5733)
C	CLOUD	4.6%	6.1%	89.3%	(34784)
		(7100)	(6890)	(31828)	(45818)

Reliability of cloud/no cloud decisions = 90.1%

() = Raw frequency

Table 3.5. Verification rates using the decision matrix on data from all orbital revolutions and manually prepared analyses as "truth".

contains normalized distributions of the results from the algorithm versus a given verified result. The rate of success (reliability) of cloud/no cloud decisions is shown at the bottom of each figure. When we computed these reliabilities, we considered clear and snow categories as cloud-free because neither one contained cloud within the IFOV. The only difference was that one contained snow and the other one did not. The overall reliability was an excellent 90.1%.

SECTION 4 - LIMITATIONS

While completing this study, we noticed several factors which limited the utility of SSC data. Limitations to using SSC data include sensor characteristics, data flow difficulties, and inherent technique limitations. The first two classes of limitations can be removed or reduced by appropriate engineering modifications to follow-on sensors. Below we discuss three aspects of the limitations due to sensor characteristics. Then, we address the data flow difficulties and irherent technique limitations.

We estimated that approximately 10% of the SSC samples which were categorized as cloudy were only partially filled with cloud. In some cases, only one L-detector pixel within the IFOV contained cloud. We learned from experience that L-detector data were much sharper than SSC data. If the SSC and L-detectors had the same resolution, there would have been less overlap of SSC cloud samples into the clear and snow categories. We believe this would improve the reliability to 95%.

During pre-launch preparations, WEC calibrated only two of the 48 detector elements of the SSC. The resultant inter-channel response to a given scene radiance varied by an estimated $\pm$5%. This inter-channel variability was small enough when compared to the wide separation between joint L-detector and SSC responses from cloud, snow (ice), and clear scenes that the affect on reliability was negligible.

The design of the SSC gain control system did not provide the capability to reduce the sensitivity of the sensor to eliminate the saturation caused by cloud-free, arid terrain features. Accordingly, we could not prove our hypothesis that the linear relationship between SSC and L-detector responses also applies to these features. As a result, our cloud/no cloud decision algorithm erroneously labeled more clear, arid features as cloudy at SSC saturation, and vice versa, than would have been the case with better gain control.

Occasionally some SSC samples were lost during playback and transmission due to noise in the recorded data. Unfortunately, we could not identify which scan lines had been lost because data time information was only provided once each minute. As a result some SSC and L-detector data were mismatched. However, we were careful to select cases for verification where this effect was minimized.

The SSC was designed to measure reflected solar, near-IR energy. As a result, we used data from daylight areas only in this study. We were not able to obtain meaningful results in areas of twilight or total darkness (i.e., areas with zero, or less, solar elevation angle.)

SECTION 5 - CONCLUSIONS

The germanium detectors were stable throughout nearly 7 months of on-orbit operation. No resolvable deterioration in the performance of the sensor occurred during this period.

Signal to noise ratios were high enough to permit processing of matching SSC and L-detector samples in daylight from near solar zenith to the terminator.

Data from a narrow-band infrared-channel centered near 1.5um, used in conjunction with L-detector data, will detect clouds with more than 90% reliability.

SECTION 6 - POTENTIAL BENEFITS

The second objective of our study was to identify potential benefits of processing snow/cloud discriminator data. Specifically, we looked for techniques and data sources to improve the Three Dimensional Nephanalysis Model (3DNEPH) and the Snow Cover Analysis Model (SNODEP). We have listed the most likely benefits in the following paragraphs.

The greatest improvement in 3DNEPH analyses would result from better detection of low stratus clouds over snow. Usually, the 3DNEPH algorithm which analyses infrared data does not detect these clouds because the temperature of the cloud tops is frequently equal to or warmer than the temperature of the underlying snow. Figure 3.12 contains a picture of nearly 26,000nm^2 of stratus clouds which the 3DNEPH algorithm would have been unable to detect. However, our cloud/no cloud decision would have detected these clouds with a reliability of better than 90%.

The greatest improvement in SNODEP analyses would result from the use of additional snow cover information in areas of the world where there are no stations reporting snow depth. The snow/no snow decision algorithm could provide snow cover information within these areas in lieu of the climatological data now used by SNODEP.

SECTION 7 - REFERENCES

Barnes, J.C., and Bowley, C.J., 1977: Study of Near-Infrared Snow Reflectance Using Skylab S192 Multispectral Scanner Data, Final Report, Contract No. 63501, Environmental Research & Technology, Inc., Concord, MA, 48 pp.

Fye, F.K., 1978: The AFGWC automated cloud analysis model. Tech Memo 78/002, AFGWC, Air Weather Service (MAC), Offutt AFB, NE, 97 pp.

Valovcin, F.R., 1976: Snow/Cloud Discrimination, Report No. AFGL-TR-76-0174, Air Force Geophysics Laboratory, Hanscom AFB, MA, 16 pp.

Valovcin, F.R., 1978: Spectral Radiance of Snow and Clouds in the Near Infrared Spectral Region, Report No. AFGL-TR-78-0289, Air Force Geophysics Laboratory, Hanscom AFB, MA, 46 pp.

AWS DISTRIBUTION

DISTRIBUTION:

1WW (10)
2WW (10)
3WW (6)
5WW (7)
7WW (5)
AWS/DNT (1)
2WS (1)
AFGWC (5)
USAFETAC/DN (2)
USAFETAC/OL-A (1)
USAFETAC/TSK (5)
AUL (1)
3350 TCHTG/TTMV (5)

END

FILMED

8-83

DTIC